Microtubules under mechanical pressure can breach dense actin networks

Matthieu Gélin, Alexandre Schaeffer, Jérémie Gaillard, Christophe Guérin, Benoit Vianay, Magali Orhant-Prioux, Marcus Braun, Christophe Leterrier, Laurent Blanchoin, Manuel Théry

Microtubules under mechanical pressure can breach dense actin networks

Matthieu Gélin, Alexandre Schaeffer, Jérémie Gaillard, Christophe Guérin, Benoit Vianay, Magali Orhant-Prioux, Marcus Braun, Christophe Leterrier, Laurent Blanchoin, Manuel Théry

© 2023. Published by The Company of Biologists Ltd | Journal of Cell Science (2023) 136, jcs261667. doi:10.1242/jcs.261667

RESEARCH ARTICLE

Microtubules under mechanical pressure can breach dense actin networks

Matthieu Gélin[1], Alexandre Schaeffer[1], Jérémie Gaillard[2], Christophe Guérin[2], Benoit Vianay[1], Magali Orhant-Prioux[2], Marcus Braun[4], Christophe Leterrier[3], Laurent Blanchoin[1,2] and Manuel Théry[1,2,*]

ABSTRACT

The crosstalk between the actin network and microtubules is essential for cell polarity. It orchestrates microtubule organization within the cell, driven by the asymmetry of actin architecture along the cell periphery. The physical intertwining of these networks regulates spatial organization and force distribution in the microtubule network. Although their biochemical interactions are becoming clearer, the mechanical aspects remain less understood. To explore this mechanical interplay, we developed an *in vitro* reconstitution assay to investigate how dynamic microtubules interact with various actin filament structures. Our findings revealed that microtubules can align and move along linear actin filament bundles through polymerization force. However, they are unable to pass through when encountering dense branched actin meshworks, similar to those present in the lamellipodium along the periphery of the cell. Interestingly, immobilizing microtubules through crosslinking with actin or other means allow the buildup of pressure, enabling them to breach these dense actin barriers. This mechanism offers insights into microtubule progression towards the cell periphery, with them overcoming obstacles within the denser parts of the actin network and ultimately contributing to cell polarity establishment.

KEY WORDS: Actin, Microtubule, Lipid, Reconstitution assays, Micropattern

INTRODUCTION

Cell polarity and internal compartmentalization depend on the interplay between actin filaments and microtubules, which are both responsible for the positioning of organelles and the organization of endomembrane networks (Bornens, 2008; Akhmanova and Kapitein, 2022). Defective coupling between actin filaments and microtubules perturb the ability of cells to sense and respond to extracellular signals due to misoriented polarity, growth and migration (Ballestrem et al., 2000; Wu et al., 2008; Zhou et al., 2002). It is thus key to understand the rules regulating the mechanical and biochemical interaction of actin filaments and microtubules. Although some shared signaling pathways have been shown to be key for their crosstalk (Krendel et al., 2002; Rooney et al., 2010), the process regulating their mechanical interaction is still unclear (Dogterom and Koenderink, 2019).

Microtubules respond specifically to different types of actin network architectures. They were described to grow along linear bundles of actin filaments (Burnette et al., 2007; Wu et al., 2008) but to be blocked by dense and branched actin meshwork in the lamellipodium (Ballestrem et al., 2000; Waterman-Storer and Salmon, 1997; Dema et al., 2023). Actin inward flow has been shown to push, reorient and even break microtubules (Gupton et al., 2002; Ning et al., 2016; Salmon et al., 2002; Schaefer et al., 2002). However, microtubule penetration through actin meshworks has been observed in neuronal growth cone (Burnette et al., 2007) and at the front of migrating epithelial cells (Wittmann et al., 2003). On one hand the frequency of these 'pioneer' or 'exploratory' microtubules was increased by actin disassembly (Burnette et al., 2007) but on the other it was reduced by Rac inactivation (Wittmann et al., 2003). Hence, the 'rules' regulating microtubule stumbling against or breaching the dense actin meshwork in the lamellipodium along cell periphery are unclear. Nonetheless, understanding the rules is key to understanding the intertwining of the two networks given that they regulate the balance of forces in the microtubule network and the orientation of cell polarity (Burute et al., 2017; Jimenez et al., 2021; Pitaval et al., 2017; Yamamoto et al., 2022) as well as the induction of membrane protrusion and directionality of cell migration (Bouchet et al., 2016; Bouchet and Akhmanova, 2017; Dema et al., 2023; Omelchenko et al., 2003; Schaefer et al., 2008).

Here, we show that the ability of microtubules to break inside a densely branched actin meshwork was not dependent on the architecture of said meshwork. In conditions where microtubules could freely move, the polymerization forces would push them rearward relative to the actin network. However, we find that, when immobilized either by mechanical hindering or by using actin–microtubule crosslinkers, microtubules could breach inside the meshwork solely due to those polymerization forces.

RESULTS

Microtubule penetration in the lamellipodium of cultured cells

When looking at microtubule organizations in mouse embryonic fibroblasts, we could clearly see microtubules aligning along stress fibers (Fig. 1A). Interestingly, these microtubules could reach the cell periphery in regions devoid of lamellipodium-like meshwork (Fig. 1A′) but were stopped in areas where such a meshwork was present (Fig. 1A″). Similarly, in fibroblast-like COS-7 cells, microtubules could barely progress up to cell periphery because of the dense actin meshwork in the lamellipodium (Fig. 1B). However, a few microtubules managed to pass through (Fig. 1B′), and this was systematic at the tips of membrane protrusions (Fig. 1B′). This clear correlation suggests that either the rare and random penetration of

[1]Université Paris cité, CEA, INSERM, Institut de Recherche Saint Louis, UMR976 HIPI, CytoMorpho Lab, Avenue Claude Vellefaux, 75010 Paris, France. [2]Université Grenoble-Alpes, CEA, CNRS, INRA, Interdisciplinary Research Institute of Grenoble, UMR5168-LPCV, CytoMorpho Lab, Avenue des Martyrs, 38054 Grenoble, France. [3]Aix Marseille Université, CNRS, INP UMR7051, NeuroCyto, 13385, Marseille, France. [4]Institute of Biotechnology, Czech Academy of Sciences, BIOCEV, 25250 Vestec, Prague West, Czech Republic.

*Author for correspondence (laurent.blanchoin@cea.fr; manuel.thery@cea.fr)

M.G., 0000-0001-5676-4841; M.B., 0000-0003-2026-2238; C.L., 0000-0002-2957-2032; M.T., 0000-0002-9968-1779

Handling Editor: Michael Way
Received 21 September 2023; Accepted 25 September 2023

Journal of Cell Science (2023) 136, jcs261667. doi:10.1242/jcs.261667

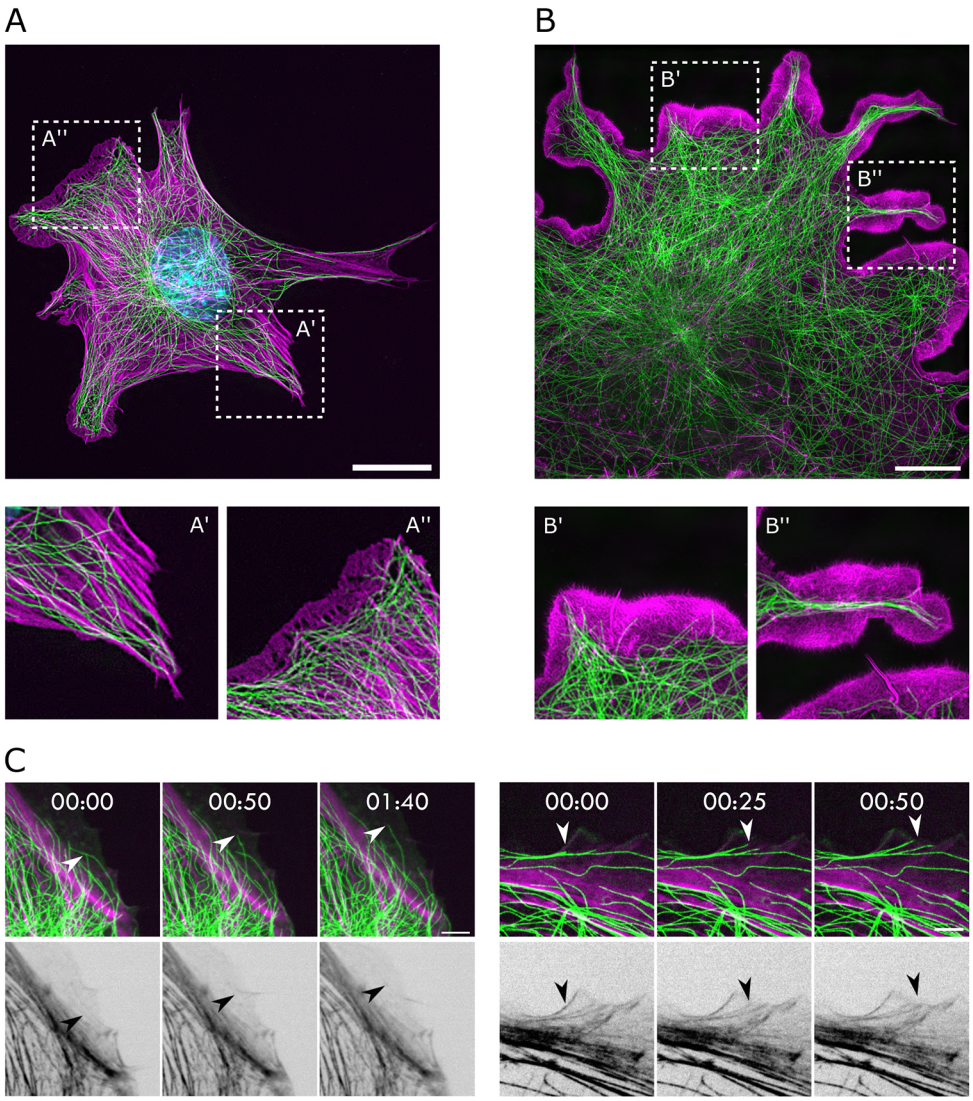

Fig. 1. Microtubule–actin interaction is structure dependent.
(A) Immunofluorescence images of the actin (magenta) and microtubule (green) network found in a MEF cell; the nucleus is in blue. Maximum projection, processing: gamma and unsharp mask. (B) Immunofluorescence images of the actin (magenta) and microtubule (green) network found in a COS-7 cell obtained by structured illumination microscopy (SIM). (C) Time-lapse of a PtK_2 cell expressing tubulin–GFP (green) incubated with 200 nM of SiR-actin (magenta). The white arrowheads highlight microtubules entering the lamellipodial region of the cell (top) and the corresponding black arrowheads highlight the actin structure encountered along their path (bottom). All images representative of 28 cells from two experimental repeats. Scale bars: 20 µm (A,B), 5 µm (C).

microtubules promotes actin reorganization in the lamellipodium and the formation of protrusions, or that a local organization of actin filaments that can promote the formation of protrusion is permissive to microtubule penetration. We could document these rare events of microtubules piercing the lamellipodium in live epithelial-like PtK_2 cells (Fig. 1C, top; Fig. S1; Movies 1, 2) expressing tubulin–GFP and labeled with SiR-actin. However, we could not identify any characteristic local feature of the actin network where microtubules breached through (Fig. 1C, bottom; Fig. S1; Movies 1, 2). In some instances, the actin network was quite homogeneous (Fig. 1C, left) whereas, in others, microtubules seemed to grow along preexisting bundles of actin filaments (Fig. 1C, right). Given that our ability to finely modulate the density and inner architecture of the lamellipodium in living cells is limited, we designed a dedicated reconstitution assay *in vitro* in order to test the role of actin network architecture in microtubule penetration.

Indeed, reconstitution assays offer the possibility of working with controlled and reproducible cytoskeleton networks. So far, they have revealed that linear actin filaments can align with and orient microtubules (Farhadi et al., 2018; Lopez and Valentine, 2016; López et al., 2014; Kučera et al., 2022b), and that branched actin filaments can limit microtubule mobility (Farhadi et al., 2020; Kučera et al., 2022a) and block their elongation (Colin et al., 2018; Inoue et al., 2019). However, these studies could not specifically address the mechanism of the piercing of dynamic microtubules into dense actin networks, which can occur in cells. This requires that microtubules and actin filaments are not randomly mixed in order for microtubules to first grow freely and then encounter dense actin meshwork. To that end, the two networks need to be spatially separated. In addition, microtubules should not be attached to the substrate so that they can move and deform freely as they encounter the actin network.

Using lipid patterning to control actin architecture

To study the interaction between dynamic microtubules and a branched actin network, we first needed a way to control the architecture of this network in a delimited space. We first used the classical approach of grafting nucleation-promoting factor (NPF, herein referring to N-WASP) on micropatterned regions on glass (Fig. 2A), as was undertaken previously (Reymann et al., 2010). Coupling that with a control of actin elongation with capping protein (CP, herein referring to CAPZ) (Boujemaa-Paterski et al., 2017), we obtained two types of actin architecture – one where the branched actin meshwork polymerized without CP and bundles could grow outside the pattern region (Fig. 2B, left), and another case where the branched actin network polymerizes in the presence of CP, which limits the

Journal of Cell Science (2023) 136, jcs261667. doi:10.1242/jcs.261667

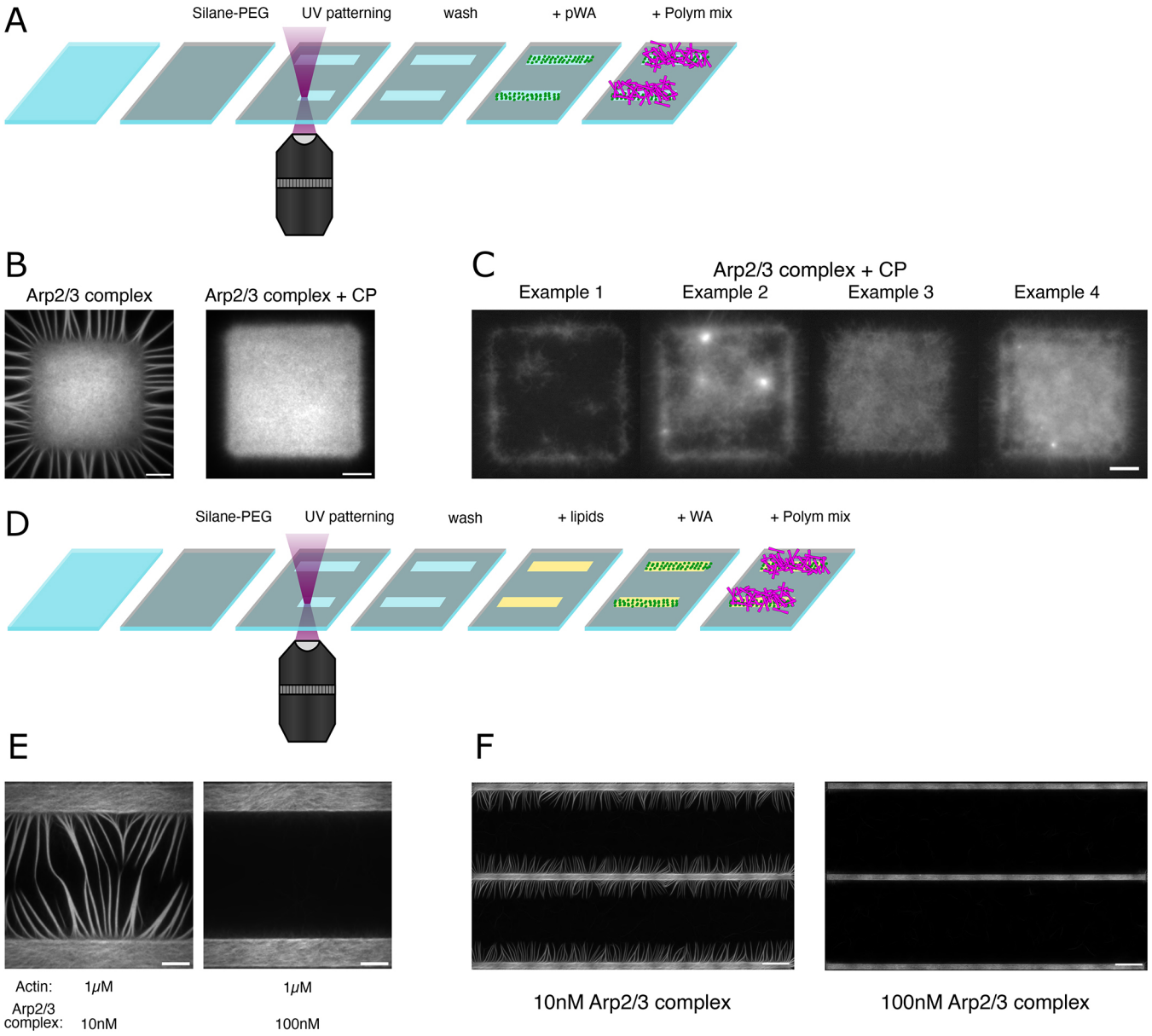

Fig. 2. Using lipid patterning to control actin architecture. (A) Scheme of the method used to pattern NPFs on glass with the PRIMO micropatterning technique. (B) Images of branched actin network polymerized from a solid patterns in presence of 100 nM of the Arp2/3 complex (left) or 100 nM of the Arp2/3 complex and 3 nM of CP (right). (C) Images of branched actin network polymerized from a solid patterns in presence of 100 nM of the Arp2/3 complex and 3 nM of CP. (D) Scheme of the method used to pattern lipids on which to graft NPFs with the PRIMO micropatterning technique. (E) Images of branched actin network polymerized from bar lipid patterns in presence of 10 nM (left) or 100 nM of the Arp2/3 complex (right). (F) Images of branched actin network polymerized from bar lipid patterns in presence of 10 nM (left) or 100 nM of the Arp2/3 complex (right). All images representative of 18 experimental repeats. Scale bars: 10 µm (B,C,E), 50 µm (F).

growth of actin bundles (Fig. 2B, right). However, the use of CP led to an irreproducibility in the growth of the meshwork. In the examples shown in Fig. 2C, the four images were taken near to each other on the same slide, yet networks displayed quite distinct densities and various internal level of heterogeneity. In an attempt to solve this reproducibility issue, we used a micropatterned lipid bilayer on which a NPF (Snap-Streptavidin-WA- His) was attached via a biotin–streptavidin link (Fig. 2D). Indeed, using NPF grafted onto a lipid bilayer can increase by a factor of 10 the efficiency of generated actin assembly compared with that of NPF grafted onto a glass micropattern (Colin et al., 2023). Unexpectedly, this method unlocked a new level of control over the branched meshwork architecture. Indeed, we found that we could alter the architecture of the meshwork simply by changing the concentration of the Arp2/3 complex and without using CP (Fig. 2E,F). At a low concentration of Arp2/3 complex (10 nM), actin filaments could grow out of the branched meshwork and form bundles. In contrast, at a higher concentration of the Arp2/3 complex (100 nM), branches were much more frequent and filaments were so numerous that they used up all the monomers, so that no filaments could grow out of the network and no outer bundles could form (Fig. 2E). In addition, the use of a lipid bilayer also solved the reproducibility issue – as the actin network was nucleated much more rapidly all over the micropatterned area, the subsequent elongation of filaments led to a fairly homogeneous network over the stretch of several hundreds of microns (Fig. 2F). These two conditions allowed us to test two characteristic architectures present at the cell periphery,

Journal of Cell Science (2023) 136, jcs261667. doi:10.1242/jcs.261667

namely dense networks of branched filaments and less-dense networks with long bundles of linear filaments, and to study their impact on the behavior of dynamic microtubules.

Alignment of dynamic microtubules along actin bundles

We then introduced free tubulin and microtubule seeds in the polymerization mix to study the interaction of dynamic microtubules with actin networks of different architectures. Microtubules exhibited normal behavior, growing and shrinking with their classical dynamic instability (Fig. 3A; Movie 3). Surprisingly, when actin bundles were present (10 nM of Arp2/3 complex), we observed an alignment between the microtubules and the bundles (Fig. 3B; Movie 4). This observation was unexpected, as no actin–microtubule crosslinkers was present in the mix, contrary to previous studies where crosslinkers were needed to observe such an alignment (Lopez and Valentine, 2016; Willige et al., 2019). The effect was quite strong and concerned the majority of the microtubules (Fig. 3C). However, given that no crosslinker was present, the microtubules were free to diffuse along the length of the actin bundles, as is seen in Fig. 3B. Importantly, the presence or absence of actin bundles had no impact on the microtubule dynamics and thus on microtubule length distribution (Fig. 3D,E).

Microtubules can breach the branched actin network

Interestingly, as growing tips of microtubules encountered the branched actin network, the force produced by their polymerization, likely by a Brownian ratchet-like mechanism (Mogilner and Oster, 2003), was strong enough to propel them backward relative to the actin network (Fig. 4A,B; Movies 5,6). Such a movement could be observed in the presence or absence of bundles, suggesting that the friction along the bundle was not sufficient to counteract the polymerization force (Fig. 4A,B; Movies 5,6). Note, in our conditions, the contact of the microtubule growing end with the actin network did not induce microtubule catastrophe (Janson et al., 2003) because the microtubule was free to move backward so the elongation of protofilament was not impaired.

We looked carefully at the growing end of the microtubule that was in contact with the actin meshwork. In the absence of an actin bundle, a microtubule never penetrated the actin meshwork (Fig. 4C). However, in the presence of actin bundles we could see some microtubules penetrating the actin meshwork (Fig. 4D). This suggests that the local organization of actin filaments at the base of the actin bundles (Svitkina et al., 2003) could be more permissive to microtubule penetration (Fig. 4E). Furthermore, the alignment of microtubules with the actin bundle could facilitate this penetration event by locking the microtubules in a favorable orientation. At the same time, we also noticed that penetration events occurred only when both ends of the microtubules were immobilized against two adjacent actin networks (asterisk at minus-end and arrowhead at plus-end in Fig. 4A). In such conditions, microtubules could not move backward, so the polymerization force puts the microtubule under pressure. Note these constrained microtubules could also pierce the meshwork from their minus end (Fig. S2). This suggested that the building up of pressure in the microtubule is responsible for their breaching through dense actin meshwork. Such a mechanism would be expected to also promote microtubule penetration in the absence of bundles. Unfortunately, the random orientation of free microtubules in the absence of actin bundle and the distance

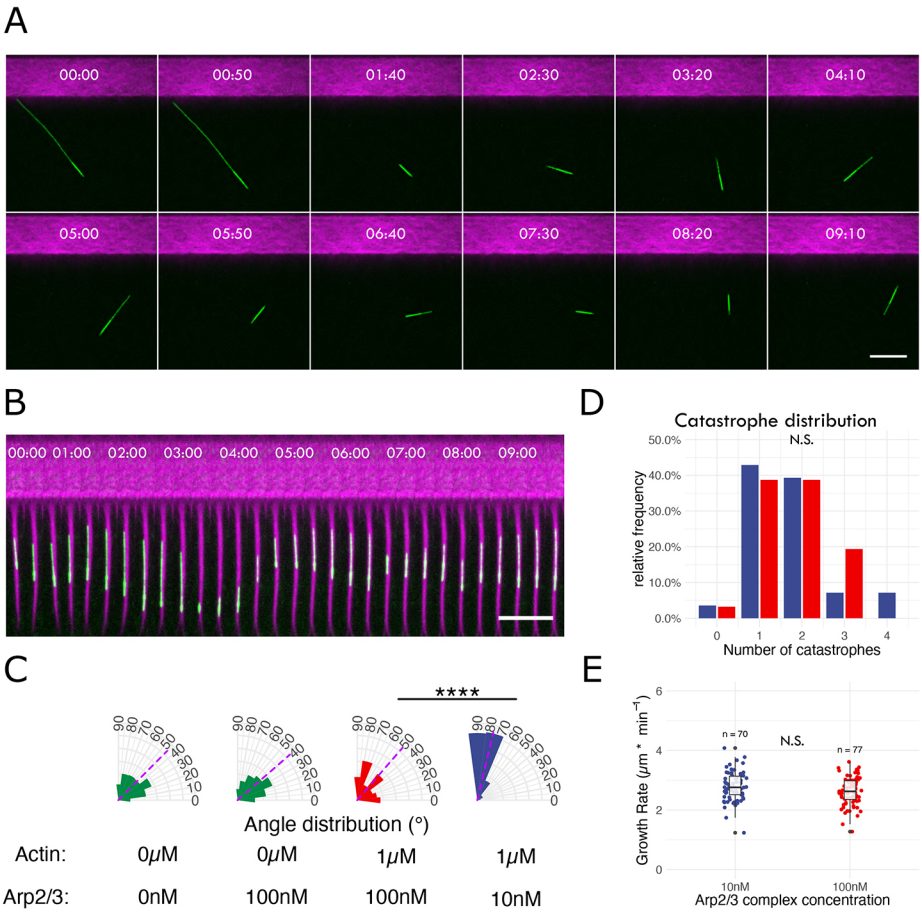

Fig. 3. Microtubule alignment along actin bundles. (A,B) Time-lapse imaging of dynamic microtubules (green) polymerizing next to a branched actin network (magenta) in absence (100 nM of Arp2/3 complex, A) or presence (10 nM of Arp2/3 complex, B) of actin bundles. (C) Distribution of microtubule orientation relative to the branched actin pattern (0 µM of actin and 0 nM of Arp2/3 complex, *n*=303, two replicates; 0 µM of actin and 100 nM of Arp2/3 complex, *n*=247, two replicates; 1 µM of actin and 100 nM of Arp2/3 complex, *n*=52, six replicates; 1 µM of actin and 10 nM of Arp2/3 complex, *n*=47, seven replicates). The magenta dashed line corresponds to the mean of the distribution. ****$P<0.0001$ (unpaired two-tailed Student's *t*-test). (D) Catastrophe distribution for microtubules interacting with the actin network in the presence (10 nM of Arp2/3 complex, blue; *n*=28, seven replicates) or absence (100 nM of Arp2/3 complex, red; *n*=31, six replicates) of actin bundles. N.S., not significant ($P>0.05$) (Fisher test). (E) Growth rate distribution of microtubule interacting with the actin network in the presence (10 nM of Arp2/3 complex, blue, *n*=70, seven replicates) or absence (100 nM of Arp2/3 complex, red, *n*=77, six replicates) of actin bundles. N.S., not significant (unpaired two-tailed Student's *t*-test). Scale bars: 10 µm (A,B).

Journal of Cell Science (2023) 136, jcs261667. doi:10.1242/jcs.261667

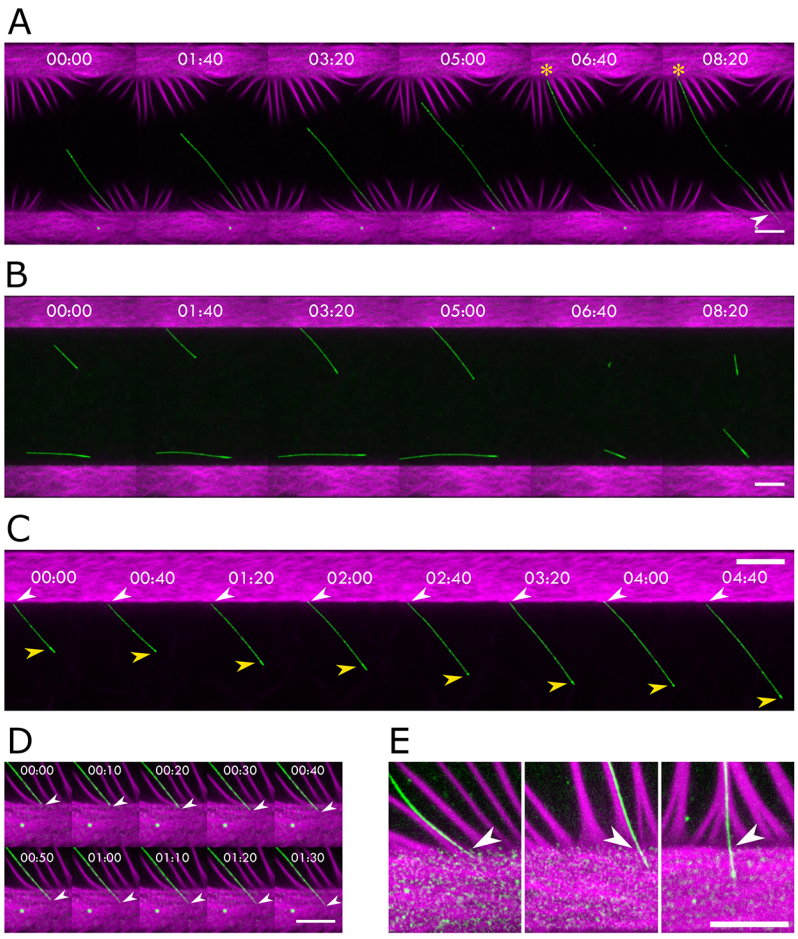

Fig. 4. Microtubule breaching inside a dense meshwork. (A) Time-lapse imaging of a dynamic microtubule (green) polymerizing in between two branched actin networks (magenta) in presence of actin bundles (10 nM of Arp2/3 complex). The yellow asterisk shows the point of contact between the minus end of the microtubule and the branched network. The white arrowhead shows the plus end of the microtubule breaching inside of the branched actin network. (B) Time-lapse imaging of dynamic microtubules (green) polymerizing in between two branched actin networks (magenta) without actin bundles (100 nM of Arp2/3 complex). (C) Magnified view of time-lapse imaging of a microtubule plus-tip (green, white arrowhead) polymerizing against a branched actin network (magenta, 100 nM of Arp2/3 complex). The yellow arrowhead indicates the microtubule seed. (D) Magnified view of time-lapse imaging of the microtubule plus-tip depicted in A (green, white arrowhead) breaching inside of the branched actin network (magenta, 10 nM of Arp2/3 complex). (E) Snapshot of multiple microtubule plus-tips (green, white arrowheads) breaching inside of branched actin networks (magenta, 10 nM of Arp2/3 complex). All images representative of 18 experimental repeats. Scale bars: 10 µm.

between the two actin meshworks did not favor such an event where both ends of microtubules were immobilized (Fig. 4B). Hence, we could not distinguish the role of pressure from the role of specific actin architecture associated with the formation of bundles.

Pressure is responsible for microtubule piercing

In order to increase the number of microtubules under pressure in the absence of actin bundles, we reduced the distance between the two micropatterned bars on which actin meshwork were nucleated (Fig. 5). In these conditions, we could observe the breaching of dynamic microtubules, even in the absence of actin bundles (yellow arrowhead in Fig. 5A; Movies 7,8). This observation shows that the specific architecture at the base of actin bundles is not necessary for microtubules to penetrate the actin network. It could nevertheless be a facilitating structure. Indeed, we observed a higher frequency of microtubules breaching the actin network in the presence of actin bundles (Fig. 5C). However, in the absence of actin bundles, a significant proportion of microtubules contacted the actin network at a low angle (<60°). (Fig. 5D). Because of their orientation, these microtubules were less likely to become long enough to make contact with the two branching networks at both ends (Fig. 5A, bottom). To compare microtubules with a similar probability to be pressurized by their growth, we selected only the microtubules that contacted the actin meshwork with an angle higher than 60° (Fig. 5E). Then, there was no more difference in the breaching probability of microtubules in the presence or absence of a bundle of actin filaments. This showed that the presence of an actin bundle did not seem to facilitate the penetration of microtubules in the actin meshwork, and that the increase of pressure in the microtubule was the main parameter responsible for these events.

Crosslinking between microtubules and actin bundles increase piercing frequency

In cells, microtubules can penetrate the lamellipodium. The local buckling of microtubules shows that they are not free to move backward as they grow against the lamellipodium (Wittmann et al., 2003; Gupton et al., 2002) and that they are likely attached to some structures that induce the build-up of pressure at the growing end. Indeed, microtubules are tethered to actin bundles or to other microtubules via specific crosslinkers (Rodriguez et al., 2003; Bodakuntla et al., 2019). We thus tested whether such crosslinkers could contribute to the build-up of pressure and to the consequent breaching of microtubules through dense actin meshwork in our *in vitro* assay. To that end, we selected the protein Tau (also known as MAPT) to crosslink microtubules with actin bundles (Elie et al., 2015; Cabrales Fontela et al., 2017) and allow the transmission of polymerization forces between the two (Alkemade et al., 2022). We worked in the 10 nM of Arp2/3 complex condition to allow actin bundles to grow out of the dense meshwork and added 100 nM of Tau to crosslink them to dynamic microtubules (Fig. 6). As expected, in the control conditions, the microtubules nicely align with the actin bundles, perpendicular to the branched network, and move backward due to the force produced by their polymerization (Fig. 6A; Movie 9). They rarely penetrate the actin network (6%, 3 out of 47 microtubules, Fig. 6B). By contrast, in the presence of Tau, microtubules could not move backward and we could detect clear

Journal of Cell Science (2023) 136, jcs261667. doi:10.1242/jcs.261667

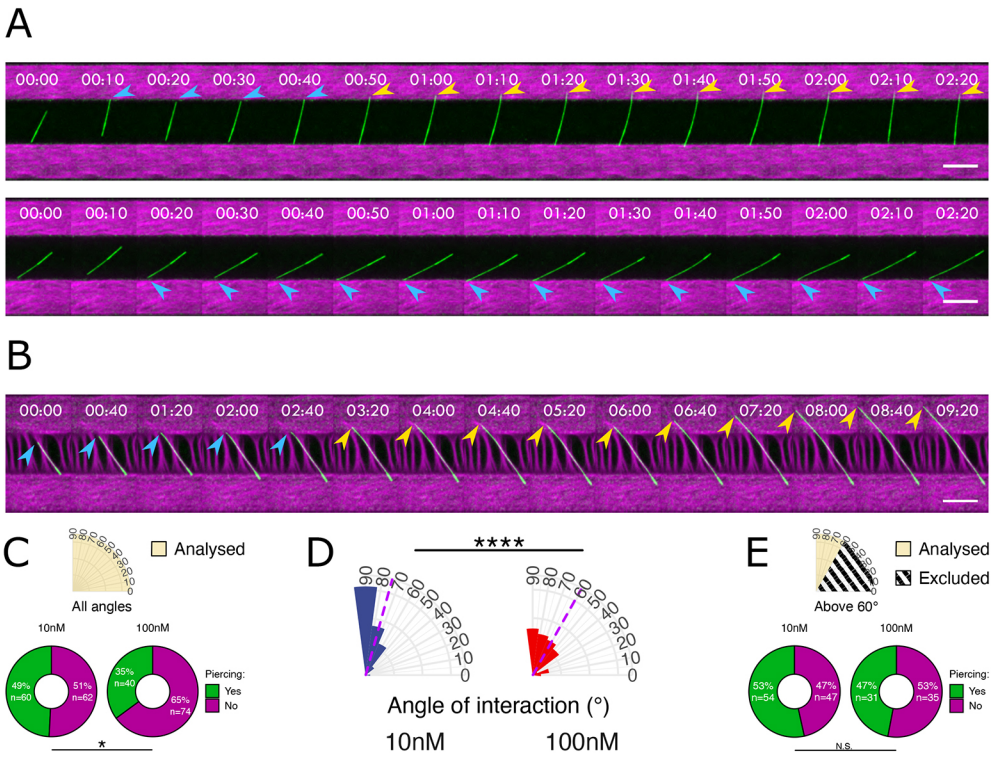

Fig. 5. Resisting load favors piercing. (A) Time-lapse imaging of dynamic microtubules (green) polymerizing in between two branched actin networks (magenta), without actin bundles (100 nM of Arp2/3 complex), at an angle lower (bottom) or greater than 60°(top). Blue arrowheads show the point of contact between microtubule plus-tip and the branched actin meshwork. Yellow arrowheads show microtubule plus-tip piercing the branched actin meshwork. (B) Time-lapse imaging of dynamic microtubules (green) polymerizing in between two branched actin networks (magenta), with actin bundles (10 nM of Arp2/3 complex). Blue arrowheads show the point of contact between microtubule plus-tip and the branched actin meshwork. Yellow arrowheads show the microtubule plus-tip piercing the branched actin meshwork. (C) Proportion of microtubules piercing the branched actin network in two different conditions: 10 nM of Arp2/3 (n=122, seven replicates) complex and 100 nM of Arp2/3 complex (n=114, six replicates). All angles were analyzed. *P<0.05 (Chi-squared test). (D) Distribution of the angle of interaction of microtubules in the presence (10 nM of Arp2/3 complex) or absence (100 nM of Arp2/3 complex) of actin bundles. The dashed magenta line corresponds to the mean of the distribution. ****P<0.0001 (unpaired two-tailed Student's t-test). (E) Proportion of microtubules piercing the branched actin network in two different conditions, 10 nM of Arp2/3 complex (n=101, seven replicates) and 100 nM of Arp2/3 complex (n=66, six replicates). Only the microtubules with an interaction angle superior to 60° were included in the analysis. N.S., not significant (P>0.05) (Chi-squared test). Scale bars: 10 µm.

beaching events (Fig. 6C; Movie 10). The frequency of these breaching events was dramatically increased by the presence of Tau (40%, 31 out of 77 microtubules, Fig. 6B). This observation might be induced by an increase in the growth rate of microtubules. However, in our case, the growth rate was significantly lowered in the presence of Tau (mean±s.d.,1.82±0.49µm/min; n= 210; Wilcoxon test P-value, 2.1×10^{-10}) as compared to the one from the control experiment (mean±s.d., 2.10±0.37µm/min; n=135). In these conditions, we cannot exclude that Tau also affected the architecture of the actin network (Elie et al., 2015). However, these results strongly suggest that the binding of microtubules to actin bundles builds up some pressure in the growing microtubule, which promotes their penetration in the densely branched actin meshwork.

DISCUSSION

Altogether, our results highlight the role of structural components, which, by resisting the backward translocation of growing microtubules, induce the build-up of pressure that push them to breach into dense actin meshworks. Our results also showed that if actin and microtubules are free to move, they will tend to align with each other even in the absence of crosslinkers. This alignment could be due to electrostatic or hydrophobic interactions (Schaedel et al., 2021). It could also result from the presence of methyl-cellulose in our polymerization mix, given that crowding agents promote the alignment of long structures through colloid osmotic pressure (Mitchison, 2019). It was tempting to speculate that this alignment guides microtubules toward regions where the organizing of actin filaments is more permissive to penetration (Schaefer et al., 2002), but, although we could not fully exclude this hypothesis, our results did not provide any evidence for such a scenario. Whether the density of branched actin meshwork in our reconstitution assay is qualitatively comparable to the lamellipodium meshwork in cells is hard to tell. However, it should be noted that the frequency of microtubules penetrating is low in both conditions, suggesting that the conditions are likely similar. Interestingly, our results show that the forces produced by microtubule polymerization are sufficient to pierce the said dense and branched actin meshwork but that counter forces are required for this to happen. This means that, in cells, the frequency of these events is under the control of the structures that can bind to microtubules and resist their backward translocation upon elongation. This suggests that the local regulation of the concentration of molecular motors, crosslinkers or other regulatory proteins might allow microtubules to breach through the lamellipodium in some specific places and thereby control the location of the delivery of specific cargoes transported along microtubules. This capacity to locally adjust signals delivery might be instrumental in the context of cell shape remodeling and migration.

Journal of Cell Science (2023) 136, jcs261667. doi:10.1242/jcs.261667

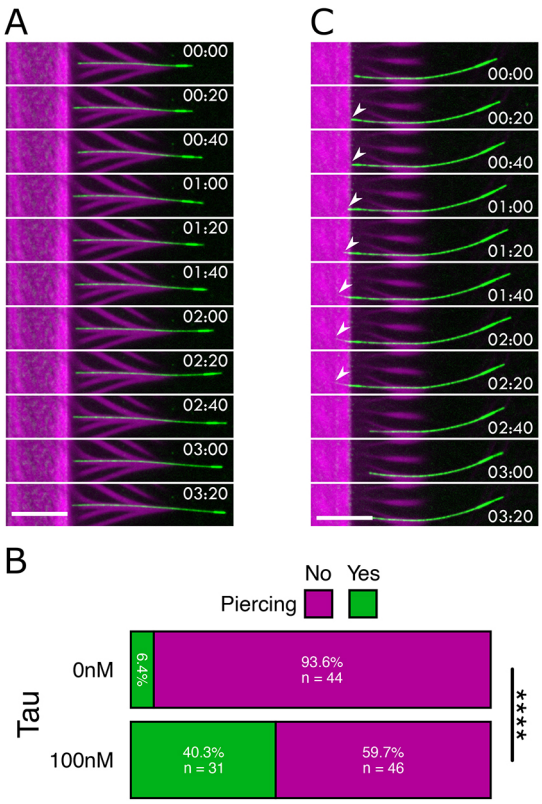

Fig. 6. The presence of crosslinker favors piercing. (A) Time-lapse imaging of dynamic microtubules (green) polymerizing against a branched actin network (magenta) in presence of actin bundles (10 nM of Arp2/3 complex). (B) Proportion of microtubules piercing the branched actin network in two different conditions: 0 nM of Tau and 100 nM of Tau. ****P<0.0001 (Chi-squared test). (C) Time-lapse imaging of dynamic microtubules (green) polymerizing against a branched actin network (magenta) in presence of actin bundles (10 nM of Arp2/3 complex, n=47, five replicates) and of an actin-microtubule crosslinker (100 nM of Tau, n=77, three replicates). White arrowheads show a microtubule plus-tip piercing the branched actin meshwork. Scale bars: 10 µm.

MATERIALS AND METHODS

Cell culture

PtK_2

Male rat kangaroo kidney epithelial cells (PtK_2) stably expressing GFP–tubulin were obtained from the laboratory of Franck Perez (UMR144, Institut Curie, France), and were grown at 37°C and 5% CO_2 in DMEM/F12 (31331028, Gibco) supplemented with 10% fetal bovine serum (10270106, Life Technologies) and 1% antibiotic-antimycotic solution (15240062, Gibco). Cells tested negative for mycoplasma.

MEFs

Wild-type mouse embryonic fibroblasts cells (MEF WT) were obtained from the laboratory of John Eriksson (Faculty of Science, Åbo Akademi University, Finland), and were grown at 37°C and 5% CO_2 in DMEM/F12 (31331028, Gibco) supplemented with 10% fetal bovine serum (10270106, Life Technologies) and 1% antibiotic-antimycotic solution (15240062, Gibco). Cells tested negative for mycoplasma.

COS-7

COS-7 cells (ATCC, ref. CRL-1651) were cultured in DMEM high glucose/Glutamax supplemented with 10% fetal bovine serum (Thermo Fisher Scientific). Fixation and staining were performed according to a previously published protocol (Jimenez et al., 2020). Briefly, cells were extracted in Triton X-100 and glutaraldehyde, then fixed using glutaraldehyde, before being quenched using $NaBH_4$, blocked and stained with anti-α-tubulin primary antibodies (monoclonal mouse clones B-5-1-2 and DM1a, 1:300, Sigma) overnight at 4°C, which were revealed with donkey anti-mouse-IgG secondary antibodies conjugated to Alexa Fluor 555 [1 h at room temperature (RT)]. To stain actin, cells were incubated for 1 h with phalloidin–Atto488 (Sigma) at the end of the staining procedure, and mounted in Prolong Glass medium (Thermo Fisher Scientific). Cells tested negative for mycoplasma.

Cell fixation and labeling of actin and microtubules

Prior to fixation MEF cells were plated overnight on glass coverslips coated with fibronectin at 10 µg/ml. Cells were fixed 10 min at RT in cytoskeleton buffer (10 mM MES, 138 mM KCl, 3 mM $MgCl_2$ and 2 mM EGTA) supplemented with 10% sucrose, 0.05% Triton X-100, 0.25% glutaraldehyde (G5882, Sigma) and 4% paraformaldehyde. Aldehyde functions were then reduced using 1 mg/ml of $NaBH_4$ for 10 min at RT. The samples were then washed three times with PBS with 0.1% Tween 20 (1379, Sigma) and incubated in a blocking solution [PBS with 0.1% Tween-20 and 3% BSA (A2153, Sigma)] for 25 min at RT. This was followed by an incubation in blocking solution at RT for 30 min with a primary antibody directed against tyrosinated tubulin (YL1/2; MAB1864, Merck) used at 1:400. The slides were then rinsed three times using PBS with 0.1% Tween 20 and incubated in blocking solution for 30 min at RT with the secondary antibody (712-545-153, Jackson ImmunoResearch) at 1:400, DAPI (D9542, Sigma) at 1:1000 and phalloidin (A34055, Life Technologies) at 1:400. Finally, the slides were rinsed twice in PBS with 0.1% Tween 20, once in PBS and mounted in Mowiol 4-88 (81381, Sigma).

Lipids and SUV preparation

L-α-phosphatidylcholine (EggPC) (Avanti, 840051C), DSPE-PEG(2000)-biotin {1,2-distearoyl-sn-glycero-3 phosphoethanolamine-N-[biotinyl (polyethylene glycol)-2000], ammonium salt, Avanti, 880129C in 10 mg chloroform} and ATTO 647N-labeled DOPE (ATTO-TEC, AD 647N-161 dehydrated) were used. Lipids were mixed in glass tubes as follows: 98.75% EggPC (10 mg/ml), 0.25% DSPE-PEG(2000)-biotin (10 mg/ml) and 1% DOPE-ATTO390 (1 mg/ml). The mixture was dried with nitrogen gas. The dried lipids were incubated under vacuum overnight. After that, the lipids were hydrated in the small unilamellar vesicle (SUV) buffer (10 mM Tris-HCl pH 7.4, 150 mM NaCl and 2 mM $CaCl_2$). The mixture was sonicated on ice for 10 min. The mixture was then centrifuged for 10 min at 20,238 ***g*** to remove large structures. The supernatants were collected and stored at 4°C until use.

Protein purification

Tubulin

Bovine brain tubulin was purified in BRB80 buffer (80 mM 1,4-piperazinediethanesulfonic acid, pH 6.8, 1 mM ethylene glycol tetra acetic acid and 1 mM $MgCl_2$) according to a previously published method (Vantard et al., 1994). Tubulin was purified from fresh bovine brain by three cycles of temperature-dependent assembly and disassembly in Brinkley Buffer 80 (BRB80 buffer; 80 mM PIPES, pH 6.8, 1 mM EGTA and 1 mM $MgCl_2$ plus 1 mM GTP) (Shelanski, 1973). MAP-free neuro-tubulin was purified by cation-exchange chromatography (EMD SO, 650 M, Merck) in 50 mM PIPES, pH 6.8, supplemented with 1 mM $MgCl_2$, and 1 mM EGTA. Purified tubulin was obtained after a cycle of polymerization and depolymerization. Microtubules were resuspended in cold BRB80. Microtubules were then depolymerized and a second cycle of polymerization and depolymerization was performed before use. Fluorescent tubulin (ATTO 488-labeled tubulin and ATTO 565-labeled tubulin) and biotinylated tubulin were prepared according to a previously published method (Hyman et al., 1991). Microtubules from neurotubulin were polymerized at 37°C for 30 min and layered onto cushions of 0.1 M NaHEPES, pH 8.6, 1 mM $MgCl_2$, 1 mM EGTA, 60% (v/v) glycerol, and sedimented at 190,000 ***g*** for 30 min at 30°C. Then microtubules were resuspended in 0.1 M NaHEPES, pH 8.6, 1 mM $MgCl_2$, 1 mM EGTA and 40% (v/v) glycerol and labeled by adding a 1/10th volume 100 mM NHS-ATTO (ATTO Tec), or

NHSBiotin (Pierce) for 10 min at 37°C. The labeling reaction was stopped using two volumes of 2× BRB80, containing 100 mM potassium glutamate and 40% (v/v) glycerol, and then microtubules were sedimented onto cushions of BRB80 supplemented with 60% glycerol. Our labeling ratio for tubulin visualization at 488 nm is 1.6 to 1.8 fluorophores per dimer, and for tubulin visualization at 565 nm, 0.6 to 0.7 fluorophores per dimer. We used NanoDrop one UV-Vis spectrophotometer (Thermofisher) to determine the labeling efficiency.

Microtubule seed preparation

Microtubule seeds were prepared at 10 µM tubulin concentration (20% ATTO-488-labeled tubulin and 80% unlabeled tubulin) in BRB80 supplemented with 0.5 mM GMPCPP at 37°C for 30 min. The seeds were incubated with 2.5 µM Taxotere (Sigma) at room temperature for 15 min and were then sedimented by ultracentrifugation (135,700 ***g***, 10 min at 25°C) and resuspended in BRB80 supplemented with 0.5 mM GMPCPP and 2.5 µM Taxotere. Finally, the seeds were flash frozen and stored at −80°C.

Actin

Actin was purified from rabbit skeletal-muscle acetone powder (Spudich and Watt, 1971). Monomeric Ca-ATP- actin was purified by gel-filtration chromatography on Sephacryl S-300 at 4°C in G-Buffer [5 mM Tris-HCl pH 8.0, 0.2 mM ATP, 0.1 mM $CaCl_2$ and 0.5 mM dithiothreitol (DTT)]. Muscle acetone powder (2 g) was suspended in 40 ml of buffer G and extracted with stirring at 4°C for 30 min, then centrifuged for 30 min at 30,000 ***g*** at 4°C. The supernatant with actin monomers was filtered through glass wool and we measured the volume. The pellets were suspended in the original volume of G-Buffer and we repeated the centrifugation and filtration steps. While stirring the combined supernatants in a beaker KCl was added to a final concentration of 50 mM and then 2 mM $MgCl_2$ to a final concentration of 2 mM. This step will polymerize the actin monomers. After 1 h, KCl was added to a final concentration of 0.8 M while stirring in a cold room. This dissociates any contaminating tropomyosin from the actin filaments. After 30 min, the solution is centrifuged for 2 h at 140,000 ***g*** to pellet the actin filaments. Then, the supernatant is discarded and the surface of the pellets gently washed with G-buffer. The pellets are gently suspended in ∼3 ml of G-buffer per original gram of acetone powder using a Dounce homogenizer and dialyzed for 2 days with three changes of G-buffer to depolymerize the actin filaments. To speed up depolymerization, the suspended actin filaments can be sonicated gently. The depolymerized actin solution is then clarified the by centrifugation in Ti45 rotor at 140,000 ***g*** for 2 h to remove aggregates. The top two-thirds of the ultracentrifuge tube contains 'conventional' actin, and gel filtering on Spectral S-300 in buffer G separates actin oligomers. Labeling was performed on lysine residues by incubating actin filaments with Alexa-Fluor-568 succimidyl ester (Molecular Probes).

Arp2/3 complex

The Arp2/3 complex was purified from calf thymus according to Egile et al. (1999) with the following modifications: the calf thymus was first mixed in an extraction buffer [20 mM Tris-HCl pH 7.5, 25 mM KCl, 1 mM $MgCl_2$, 0.5 mM EDTA, 5% glycerol, 1 mM DTT, 0.2 mM ATP 1 mM PMSF and 1× EDTA-free Protease Inhibitor Cocktail (Sigma, ref. 11836170001)]. Then, it was placed in a 50% ammonium sulfate solution in order to make the proteins precipitate. The pellet was resuspended in extraction buffer and dialyzed overnight. The Arp2/3 complex was fluorescently labeled as described in Funk et al. (2021).

Human profilin

Human profilin was expressed in BL21 DE3 pLys *Escherichia coli* cells and purified according to Almo et al. (1994).

Streptavidin-WA

Snap-Streptavidin-WA-His (pETplasmid; Sigma, ref. 69909) was expressed in Rosetta 2 (DE3) pLysS (Merck, 71403). Culture was grown in TB medium supplemented with 30 µg/ml kanamycin and 34 µg/ml chloramphenicol, then 0.5 mM isopropyl β-D-1-thiogalactopyranoside (IPTG) was added, and protein was expressed overnight at 16°C. Pelleted cells (5000 ***g*** for 30 min) were resuspended in lysis buffer (20 mM Tris-HCl pH 8, 500 mM NaCl, 1 mM EDTA, 15 mM imidazole, 0.1% Triton X-100, 5% glycerol and 1 mM DTT). Following sonication (4 min, 40% at 4°C) and centrifugation (16,000 ***g*** for 30 min at 4°C), the clarified extract was loaded on a Ni Sepharose high-performance column (GE Healthcare Life Sciences, ref 17526802). Resin was washed with wash buffer (20 mM Tris-HCl pH 8, 500 mM NaCl, 1 mM EDTA, 30 mM imidazole and 1 mM DTT). Protein was eluted with elution buffer (20 mM Tris-HCl pH 8, 500 mM NaCl, 1 mM EDTA, 300 mM imidazole and 1 mM DTT). Purified protein was dialyzed overnight 4°C with storage buffer (20 mM Tris-HCl pH 8, 150 mM NaCl, 1 mM EDTA and 1 mM DTT), concentrated with an Amicon 3KD kit (Merck, UFC900324) to obtain concentration around 10 µM then centrifuged at 160,000 ***g*** for 30 min. Aliquots were flash-frozen in liquid nitrogen and stored at −80°C.

Glass passivation

The micropatterning technique was adapted from Portran et al. (2013). Cover glasses were cleaned by successive chemical treatments: 30 min in acetone, 15 min in ethanol (96%), rinsing in ultrapure water, 2 h in Hellmanex III (2% in water, Hellmanex), and rinsing in ultrapure water. Cover glasses were dried using filtered air flow, oxidized using air plasma during 5 min (400 W, PlasmaEtch), and incubated at least overnight in a solution of tri-ethoxysilane-PEG (5 kDa for coverslip and 30 kDa for slides, Creative PEGWorks) at 1 mg/ml in ethanol 96% and 0.1% HCl, with gentle agitation at room temperature. Cover glasses were kept in solution at room temperature and stored until use. When used, the cover glasses were successively washed in ethanol, ultrapure water and dried with filtered air.

Glass micropatterning

A chamber made of a passivated coverslip and cover glass was mounted using some double-sided tape (70 µm height). This chamber was then perfused with a photoinitiator solution (PLPP, Alveole) and transferred on an inverted microscope (Ti-E, Nikon) equipped with the PRIMO system (Alveole). The alignment of the motorized stage with the camera and calibration of the Digital Micromirror Device (DMD) with the camera was undertaken using the Leonardo software (Alveole) (Strale et al., 2016). We used a dose of 100 mJ/mm^2 of UV to create micropatterns on silane-PEG (30 kDa). After UV exposure, the chamber was rinsed using a SUV buffer (10 mM Tris-HCl pH 7.4, 150 mM NaCl and 2 mM $CaCl_2$).

Streptavidin-WA grafting on micropatterned lipid biotin

The SUVs, containing lipids and lipid-biotins, were introduced in the newly micropatterned chamber and incubated for 10 min, followed by several washing steps with the SUV buffer and another washing using the 'wash buffer' solution composed of a mix of 1× HKEM (10 mM HEPES pH 7.5, 50 mM KCl, 5 mM $MgCl_2$ and 1 mM EGTA) and 1× G-buffer (2 mM Tris-HCl pH 8.0, 0.2 mM

ATP, 0.1 mM $CaCl_2$ and 0.5 mM DTT). Next, a dilution of streptavidin-WA (100 nM in wash buffer) was incubated for 3 min. A final rinse was undertaken using the wash buffer.

Co-assembly of actin filaments and microtubules

All components necessary for actin filaments and microtubule growth were added together in 'Tic-Tac' buffer (10 mM Hepes, 16 mM Pipes pH 6.8, 50 mM KCl, 1 mM EGTA, 5 mM $MgCl_2$) with Actin (1 µM), the Arp2/3 complex (at 10 nM or 100 nM), human profilin (2 µM), tubulin (17 µM), microtubule seeds (1:750 dilution in wash buffer) and Tau (100 nM; from the laboratory of Lansky and Braun, BIOCEV, Czech Republic).

Microscopic observation

TIRF imaging

Imaging of experiments involving microtubules were performed on an inverted microscope (Ti-E, Nikon), equipped with a total internal reflection fluorescence (TIRF) iLasPulsed system (Gataca Systems) and a Retiga R3 camera (CCD 1920×1460, Binning=1, pixel=4.54 µm) using an Olympus U APO N TIRF oil-immersion 100×1.49 NA objective lens, with a 0.63 O ring. The microscope stage was maintained at 37°C by means of a temperature controller to obtain an optimal microtubule growth. Multi-stage time-lapse movies were acquired using Metamorph software (version, Universal Imaging).

For experiments involving the observation of large patterns over the course of an experiment, a custom stage list was created using the scan slide journal of Metamorph and the origin of the stage was setup as the top right corner of the pattern.

To increase the signal-to-noise ratio of the tubulin channel, a background subtraction was performed (rolling ball radius=20). The growth rate, catastrophe frequency, angle distribution and piercing frequency of the microtubules was manually measured using Fiji software.

Imaging of fixed samples

Acquisition of fixed samples were made with an inverted microscope (Ti-E, Nikon), equipped with a spinning disk confocal csu (Yokogawa CSU-X1), iLasPulsed system (Gataca Systems) and a Retiga R3 camera (CCD 1920×1460, Binning=2, pixel=4.54 µm) using a Nikon plan APO VC oil-immersion 60×1.40 NA objective lens. Multi-stage *Z*-series acquisitions were done using Metamorph software (version 7.7.11.0, Universal Imaging). A maximum *Z*-projection was performed alongside gamma processing for the actin channel (value=0.6) and unsharp mask for the tubulin channel (radius=1, mask weight=0.7).

Live imaging of actin and microtubules in cells

PtK_2 cells were plated overnight in glass bottom dishes (627860, Dutscher) coated with fibronectin and collagen both at 10 µg/ml. Cells were then treated for 4 h with SiR-Actin (SC001, tebubio) at concentrations between 200 and 300 nM, and Verapamil (SC001, tebubio) at concentrations between 10 and 15 µM. Live acquisitions of endogenously expressed GFP tubulin and filamentous actin stained with SIR-Actin were made inside a live module (kept at 37°C and 5% CO_2) mounted on a confocal spinning disk microscope (Nikon Ti Eclipse equipped with a spinning scanning unit CSU-X1 Yokogawa) and a R3 retiga camera (QImaging). Images were acquired using a Nikon Plan Apo VC 60×/1.40 NA oil objective. Each wavelength was acquired separately.

Metamorph software was used for image acquisition (version 7.7.11.0, Universal Imaging).

SIM imaging

Cells were imaged on a N-SIM-S microscope (Nikon) using a classical three-beam configuration for 3D-SIM. A laser at 488 nm (for actin) and 561 nm (for microtubules) was used to illuminate the sample through a 100×1.49 NA objective, capturing 15 images (16-bit, 1024×1024 pixels at 65 nm/pixel) over a 50 to 100 ms exposure time via a Fusion BT sCMOS camera (Hamamatsu). The raw images were then processed using the N-SIM module of the NIS Elements software, resulting in a 32-bit, 2048×2048 pixel reconstructed image at 32.5 nm/pixel. Images were converted into 16 bit, projected, overlayed and contrast-adjusted in Fiji software.

Statistical analysis

All the graphs and statistical analysis were performed using R software (https://www.r-project.org/).

Acknowledgement

We would like to thank the Neuro-Cellular Imaging Service and Nikon Center for Neuro-NanoImaging at INP as well as the Institut Marseille Imaging centre for complementary equipment. The MuLife imaging facility is funded by GRAL, a program from the Chemistry Biology Health Graduate School of University Grenoble Alpes (ANR-17-EURE-0003). The Neuro-Cellular Imaging Service and Nikon Center for Neuro-NanoImaging at INP is supported by CPER-FEDER (PlateForme NeuroTimone PA0014842). The Institut Marseille Imaging centre is supported by from Excellence Initiative of Aix-Marseille University – A*MIDEX, a French 'Investissements d'Avenir' programme (AMX-19- IET-002).

Competing interests

The authors declare no competing or financial interests.

Author contributions

Conceptualization: L.B., M.T.; Methodology: J.G., C.G., B.V., M.O.-P.; Validation: L.B., M.T.; Formal analysis: M.G.; Investigation: M.G., L.B., M.T.; Resources: M.B., C.L.; Data curation: M.G., A.S.; Writing - original draft: M.G., M.T.; Writing - review & editing: M.G., L.B., M.T.; Supervision: L.B., M.T.; Project administration: L.B.; Funding acquisition: L.B., M.T.

Funding

This work was supported by the European Research Council [Consolidator Grant 771599 (ICEBERG) to M.T. and Advanced Grant 741773 (AAA) to L.B.].

Data availability

All relevant data can be found within the article and its supplementary information. The corresponding authors, upon reasonable request, will share the raw data used to reach the conclusions reported in this paper.

Peer review history

The peer review history is available online at https://journals.biologists.com/jcs/lookup/doi/10.1242/jcs.261667.reviewer-comments.pdf

References

Akhmanova, A. and Kapitein, L. C. (2022). Mechanisms of microtubule organization in differentiated animal cells. *Nat. Rev. Mol. Cell Biol.* **23**, 541-558. doi:10.1038/s41580-022-00473-y

Alkemade, C., Wierenga, H., Volkov, V. A., López, M. P., Akhmanova, A., Ten Wolde, P. R., Dogterom, M. and Koenderink, G. H. (2022). Cross-linkers at growing microtubule ends generate forces that drive actin transport. *Proc. Natl. Acad. Sci. USA* **119**, e2112799119. doi:10.1073/pnas.2112799119

Almo, S. C., Pollard, T. D., Way, M. and Lattman, E. E. (1994). Purification, characterization and crystallization of Acanthamoeba profilin expressed in Escherichia coli. *J. Mol. Biol.* **236**, 950-952. doi:10.1006/jmbi.1994.1200

Ballestrem, C., Wehrle-Haller, B., Hinz, B. and Imhof, B. A. (2000). Actin-dependent lamellipodia formation and microtubule-dependent tail retraction control-directed cell migration. *Mol. Biol. Cell* **11**, 2999-3012. doi:10.1091/mbc.11.9.2999

Bodakuntla, S., Jijumon, A. S., Villablanca, C., Gonzalez-Billault, C. and Janke, C. (2019). Microtubule-associated proteins: structuring the cytoskeleton. *Trends Cell Biol.* **29**, 804-819. doi:10.1016/j.tcb.2019.07.004

Bornens, M. (2008). Organelle positioning and cell polarity. *Nat. Rev. Mol. Cell Biol.* **9**, 874-886. doi:10.1038/nrm2524

Bouchet, B. P. and Akhmanova, A. (2017). Microtubules in 3D cell motility. *J. Cell Sci.* **130**, 39-50. doi:10.1242/jcs.189431

Bouchet, B. P., Noordstra, I., Van Amersfoort, M., Katrukha, E. A., Ammon, Y.-C., Ter Hoeve, N. D., Hodgson, L., Dogterom, M., Derksen, P. W. B. and Akhmanova, A. (2016). Mesenchymal cell invasion requires cooperative regulation of persistent microtubule growth by SLAIN2 and CLASP1. *Dev. Cell* **39**, 708-723. doi:10.1016/j.devcel.2016.11.009

Boujemaa-Paterski, R., Suarez, C., Klar, T., Zhu, J., Guérin, C., Mogilner, A., Théry, M. and Blanchoin, L. (2017). Network heterogeneity regulates steering in actin-based motility. *Nat. Commun.* **8**, 655. doi:10.1038/s41467-017-00455-1

Burnette, D. T., Schaefer, A. W., Ji, L., Danuser, G. and Forscher, P. (2007). Filopodial actin bundles are not necessary for microtubule advance into the peripheral domain of aplysia neuronal growth cones. *Nat. Cell Biol.* **9**, 1360-1369. doi:10.1038/ncb1655

Burute, M., Prioux, M., Blin, G., Truchet, S., Letort, G., Tseng, Q., Bessy, T., Lowell, S., Young, J., Filhol, O. et al. (2017). Polarity reversal by centrosome repositioning primes cell scattering during epithelial-to-mesenchymal transition. *Dev. Cell* **40**, 168-184. doi:10.1016/j.devcel.2016.12.004

Cabrales Fontela, Y., Kadavath, H., Biernat, J., Riedel, D., Mandelkow, E. and Zweckstetter, M. (2017). Multivalent cross-linking of actin filaments and microtubules through the microtubule-associated protein Tau. *Nat. Commun.* **8**, 1981. doi:10.1038/s41467-017-02230-8

Colin, A., Singaravelu, P., Théry, M., Blanchoin, L. and Gueroui, Z. (2018). Actin-network architecture regulates microtubule dynamics. *Curr. Biol.* **28**, 2647-2656.e4. doi:10.1016/j.cub.2018.06.028

Colin, A., Orhant-Prioux, M., Guérin, C., Savinov, M., Cao, W., Vianay, B., Scarfone, I., Roux, A., De La Cruz, E. M., Mogilner, A. et al. (2023). Friction patterns guide actin network contraction. *Proc. Natl. Acad. Sci. USA* **120**, e2300416120. doi:10.1073/pnas.2300416120

Dema, A., Charafeddine, R., Rahgozar, S., Van Haren, J. and Wittmann, T. (2023). Growth cone advance requires EB1 as revealed by genomic replacement with a light-sensitive variant. *Elife* **12**, e84143. doi:10.7554/eLife.84143

Dogterom, M. and Koenderink, G. H. (2019). Actin–microtubule crosstalk in cell biology. *Nat. Rev. Mol. Cell Biol.* **20**, 38-54. doi:10.1038/s41580-018-0067-1

Egile, C., Loisel, T. P., Laurent, V., Li, R., Pantaloni, D., Sansonetti, P. J. and Carlier, M.-F. (1999). Activation of the Cdc42 effector N-Wasp by the Shigella flexneri Icsa protein promotes actin nucleation by Arp2/3 complex and bacterial actin-based motility. *J. Cell Biol.* **146**, 1319-1332. doi:10.1083/jcb.146.6.1319

Elie, A., Prezel, E., Guérin, C., Denarier, E., Ramirez-Rios, S., Serre, L., Andrieux, A., Fourest-Lieuvin, A., Blanchoin, L. and Arnal, I. (2015). Tau co-organizes dynamic microtubule and actin networks. *Sci. Rep.* **5**, 9964. doi:10.1038/srep09964

Farhadi, L., Do Rosario, C. F., Debold, E. P., Baskaran, A. and Ross, J. L. (2018). Active self-organization of actin-microtubule composite self-propelled rods. *Front. Phys.* **6**, 75. doi:10.3389/fphy.2018.00075

Farhadi, L., Ricketts, S. N., Rust, M. J., Das, M., Robertson-Anderson, R. M. and Ross, J. L. (2020). Actin and microtubule crosslinkers tune mobility and control co-localization in a composite cytoskeletal network. *Soft Mat.* **16**, 7191-7201. doi:10.1039/C9SM02400J

Funk, J., Merino, F., Schaks, M., Rottner, K., Raunser, S. and Bieling, P. (2021). A barbed end interference mechanism reveals how capping protein promotes nucleation in branched actin networks. *Nat. Commun.* **12**, 5329. doi:10.1038/s41467-021-25682-5

Gupton, S. L., Salmon, W. C. and Waterman-Storer, C. M. (2002). Converging populations of F-actin promote breakage of associated microtubules to spatially regulate microtubule turnover in migrating cells. *Curr. Biol.* **12**, 1891-1899. doi:10.1016/S0960-9822(02)01276-9

Hyman, A., Drechsel, D., Kellogg, D., Salser, S., Sawin, K., Steffen, P., Wordeman, L. and Mitchison, T. (1991). [39] Preparation of modified tubulins. *Methods Enzymol.* **196**, 478-485. doi:10.1016/0076-6879(91)96041-O

Inoue, D., Obino, D., Pineau, J., Farina, F., Gaillard, J., Guerin, C., Blanchoin, L., Lennon-Duménil, A.-M. and Théry, M. (2019). Actin filaments regulate microtubule growth at the centrosome. *EMBO J.* **38**, e99630. doi:10.15252/embj.201899630

Janson, M. E., De Dood, M. E. and Dogterom, M. (2003). Dynamic instability of microtubules is regulated by force. *J. Cell Biol.* **161**, 1029-1034. doi:10.1083/jcb.200301147

Jimenez, A., Friedl, K. and Leterrier, C. (2020). About samples, giving examples: optimized single molecule localization microscopy. *Methods* **174**, 100-114. doi:10.1016/j.ymeth.2019.05.008

Jimenez, A. J., Schaeffer, A., De Pascalis, C., Letort, G., Vianay, B., Bornens, M., Piel, M., Blanchoin, L. and Théry, M. (2021). Acto-myosin network geometry defines centrosome position. *Curr. Biol.* **31**, 1206-1220.e5. doi:10.1016/j.cub.2021.01.002

Krendel, M., Zenke, F. T. and Bokoch, G. M. (2002). Nucleotide exchange factor GEF-H1 mediates cross-talk between microtubules and the actin cytoskeleton. *Nat. Cell Biol.* **4**, 294-301. doi:10.1038/ncb773

Kučera, O., Gaillard, J., Guérin, C., Théry, M. and Blanchoin, L. (2022a). Actin–microtubule dynamic composite forms responsive active matter with memory. *Proc. Natl. Acad. Sci. USA* **119**, e2209522119. doi:10.1073/pnas.2209522119

Kučera, O., Gaillard, J., Guérin, C., Utzschneider, C., Théry, M. and Blanchoin, L. (2022b). Actin architecture steers microtubules in active cytoskeletal composite. *Nano Lett.* **22**, 8584-8591. doi:10.1021/acs.nanolett.2c03117

Lopez, B. J. and Valentine, M. T. (2016). The +TIP coordinating protein EB1 is highly dynamic and diffusive on microtubules, sensitive to GTP analog, ionic strength, and EB1 concentration. *Cytoskeleton* **73**, 23-34. doi:10.1002/cm.21267

López, M. P., Huber, F., Grigoriev, I., Steinmetz, M. O., Akhmanova, A., Koenderink, G. H. and Dogterom, M. (2014). Actin–microtubule coordination at growing microtubule ends. *Nat. Commun.* **5**, 4778. doi:10.1038/ncomms5778

Mitchison, T. J. (2019). Colloid osmotic parameterization and measurement of subcellular crowding. *Mol. Biol. Cell* **30**, 173-180. doi:10.1091/mbc.E18-09-0549

Mogilner, A. and Oster, G. (2003). Force generation by actin polymerization II: the elastic ratchet and tethered filaments. *Biophys. J.* **84**, 1591-1605. doi:10.1016/S0006-3495(03)74969-8

Ning, W., Yu, Y., Xu, H., Liu, X., Wang, D., Wang, J., Wang, Y. and Meng, W. (2016). The CAMSAP3-ACF7 complex couples noncentrosomal microtubules with actin filaments to coordinate their dynamics. *Dev. Cell* **39**, 61-74. doi:10.1016/j.devcel.2016.09.003

Omelchenko, T., Vasiliev, J. M., Gelfand, I. M., Feder, H. H. and Bonder, E. M. (2003). Rho-dependent formation of epithelial "leader" cells during wound healing. *Proc. Natl Acad. Sci. USA* **100**, 10788-10793. doi:10.1073/pnas.1834401100

Pitaval, A., Senger, F., Letort, G., Gidrol, X., Guyon, L., Sillibourne, J. and Théry, M. (2017). Microtubule stabilization drives 3D centrosome migration to initiate primary ciliogenesis. *J. Cell Biol.* **216**, 3713-3728. doi:10.1083/jcb.201610039

Portran, D., Gaillard, J., Vantard, M. and Thery, M. (2013). Quantification of MAP and molecular motor activities on geometrically controlled microtubule networks. *Cytoskeleton* **70**, 12-23. doi:10.1002/cm.21081

Reymann, A.-C., Martiel, J.-L., Cambier, T., Blanchoin, L., Boujemaa-Paterski, R. and Théry, M. (2010). Nucleation geometry governs ordered actin networks structures. *Nat. Mater.* **9**, 827-832. doi:10.1038/nmat2855

Rodriguez, O. C., Schaefer, A. W., Mandato, C. A., Forscher, P., Bement, W. M. and Waterman-Storer, C. M. (2003). Conserved microtubule–actin interactions in cell movement and morphogenesis. *Nat. Cell Biol.* **5**, 599-609. doi:10.1038/ncb0703-599

Rooney, C., White, G., Nazgiewicz, A., Woodcock, S. A., Anderson, K. I., Ballestrem, C. and Malliri, A. (2010). The Rac activator STEF(Tiam2) regulates cell migration by microtubule-mediated focal adhesion disassembly. *EMBO Rep.* **11**, 292-298. doi:10.1038/embor.2010.10

Salmon, W. C., Adams, M. C. and Waterman-Storer, C. M. (2002). Dual-wavelength fluorescent speckle microscopy reveals coupling of microtubule and actin movements in migrating cells. *J. Cell Biol.* **158**, 31-37. doi:10.1083/jcb.200203022

Schaedel, L., Lorenz, C., Schepers, A. V., Klumpp, S. and Köster, S. (2021). Vimentin intermediate filaments stabilize dynamic microtubules by direct interactions. *Nat. Commun.* **12**, 3799. doi:10.1038/s41467-021-23523-z

Schaefer, A. W., Kabir, N. and Forscher, P. (2002). Filopodia and actin arcs guide the assembly and transport of two populations of microtubules with unique dynamic parameters in neuronal growth cones. *J. Cell Biol.* **158**, 139-152. doi:10.1083/jcb.200203038

Schaefer, A. W., Schoonderwoert, V. T. G., Ji, L., Mederios, N., Danuser, G. and Forscher, P. (2008). Coordination of actin filament and microtubule dynamics during neurite outgrowth. *Dev. Cell* **15**, 146-162. doi:10.1016/j.devcel.2008.05.003

Shelanski, M. L. (1973). Chemistry of the filaments and tubules of brain. *J. Histochem. Cytochem.* **21**, 529-539. doi:10.1177/21.6.529

Spudich, J. A. and Watt, S. (1971). The regulation of rabbit skeletal muscle contraction. *J. Biol. Chem.* **246**, 4866-4871. doi:10.1016/S0021-9258(18)62016-2

Strale, P.-O., Azioune, A., Bugnicourt, G., Lecomte, Y., Chahid, M. and Studer, V. (2016). Multiprotein printing by light-induced molecular adsorption. *Adv. Mater.* **28**, 2024-2029. doi:10.1002/adma.201504154

Svitkina, T. M., Bulanova, E. A., Chaga, O. Y., Vignjevic, D. M., Kojima, S.-I., Vasiliev, J. M. and Borisy, G. G. (2003). Mechanism of filopodia initiation by reorganization of a dendritic network. *J. Cell Biol.* **160**, 409-421. doi:10.1083/jcb.200210174

Vantard, M., Peter, C., Fellous, A., Schellenbaum, P. and Lambert, A.-M. (1994). Characterization of a 100-KDa heat-stable microtubule-associated protein from higher plants. *Eur. J. Biochem.* **220**, 847-853. doi:10.1111/j.1432-1033.1994.tb18687.x

Waterman-Storer, C. M. and Salmon, E. D. (1997). Actomyosin-based retrograde flow of microtubules in the lamella of migrating epithelial cells influences microtubule dynamic instability and turnover and is associated with microtubule breakage and treadmilling. *J. Cell Biol.* **139**, 417-434. doi:10.1083/jcb.139.2.417

Willige, D., Hummel, J. J. A., Alkemade, C., Kahn, O. I., Au, F. K. C., Qi, R. Z., Dogterom, M., Koenderink, G. H., Hoogenraad, C. C. and Akhmanova, A. (2019). Cytolinker Gas2L1 regulates axon morphology through microtubule-modulated actin stabilization. *EMBO Rep.* **20**, e47732. doi:10.15252/embr.201947732

Wittmann, T., Bokoch, G. M. and Waterman-Storer, C. M. (2003). Regulation of leading edge microtubule and actin dynamics downstream of Rac1. *J. Cell Biol.* **161**, 845-851. doi:10.1083/jcb.200303082

Wu, X., Kodama, A. and Fuchs, E. (2008). ACF7 regulates cytoskeletal-focal adhesion dynamics and migration and has ATPase activity. *Cell* **135**, 137-148. doi:10.1016/j.cell.2008.07.045

Yamamoto, S., Gaillard, J., Vianay, B., Guerin, C., Orhant-Prioux, M., Blanchoin, L. and Théry, M. (2022). Actin network architecture can ensure robust centering or sensitive decentering of the centrosome. *EMBO J.* **41**, e111631. doi:10.15252/embj.2022111631

Zhou, F.-Q., Waterman-Storer, C. M. and Cohan, C. S. (2002). Focal loss of actin bundles causes microtubule redistribution and growth cone turning. *J. Cell Biol.* **157**, 839-849. doi:10.1083/jcb.200112014

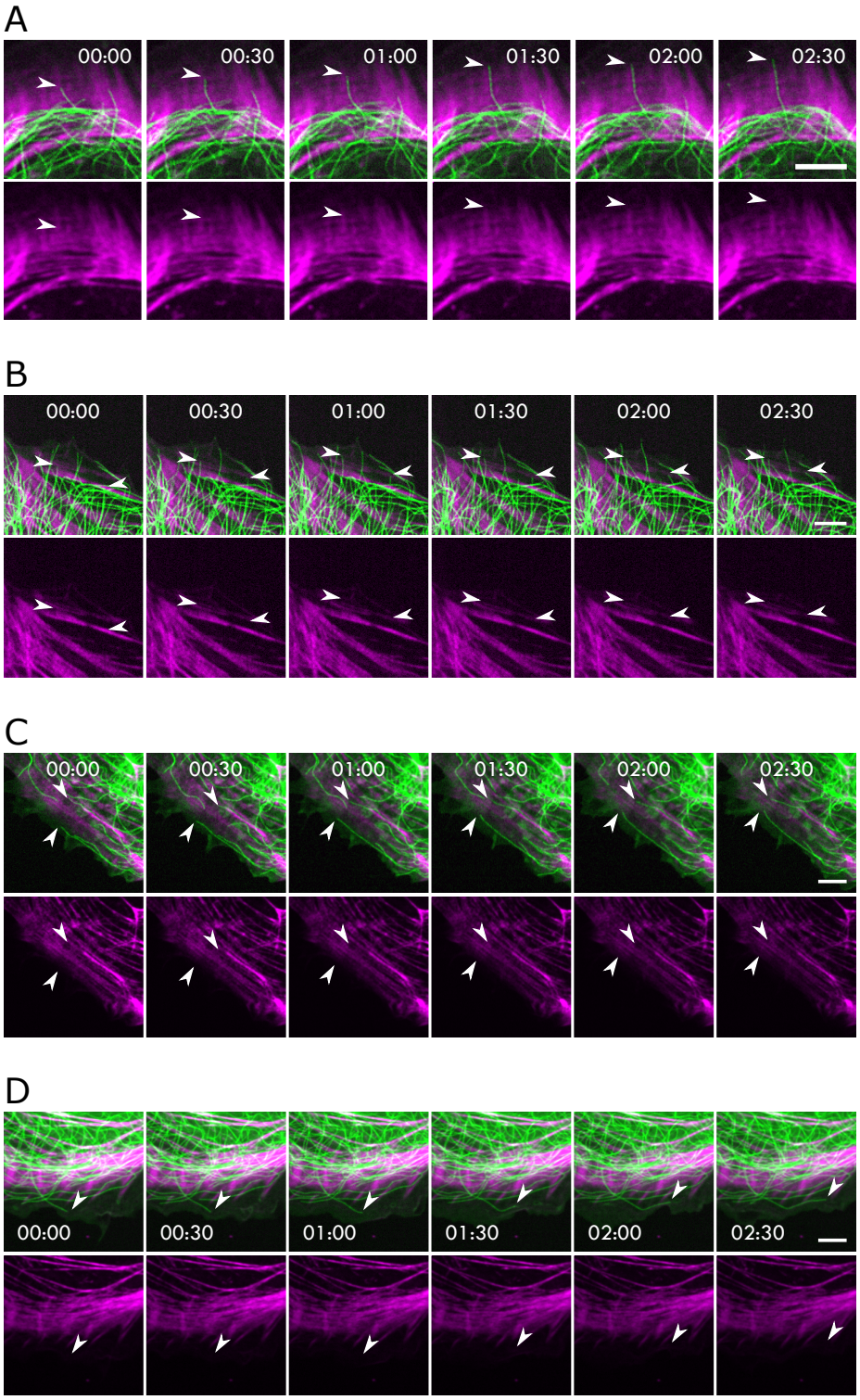

Fig. S1. Examples of microtubules entering the lamellipodial region of cells. (**A-B-C-D**) Time-lapses of a PtK_2 cell tubulin-GFP (green) incubated with 200nM of SiR-actin (magenta). The white arrows are showing microtubules entering the lamellipodial region of the cell (Top) and the actin structure encountered along their path (bottom). Scale bar, 5 µm.

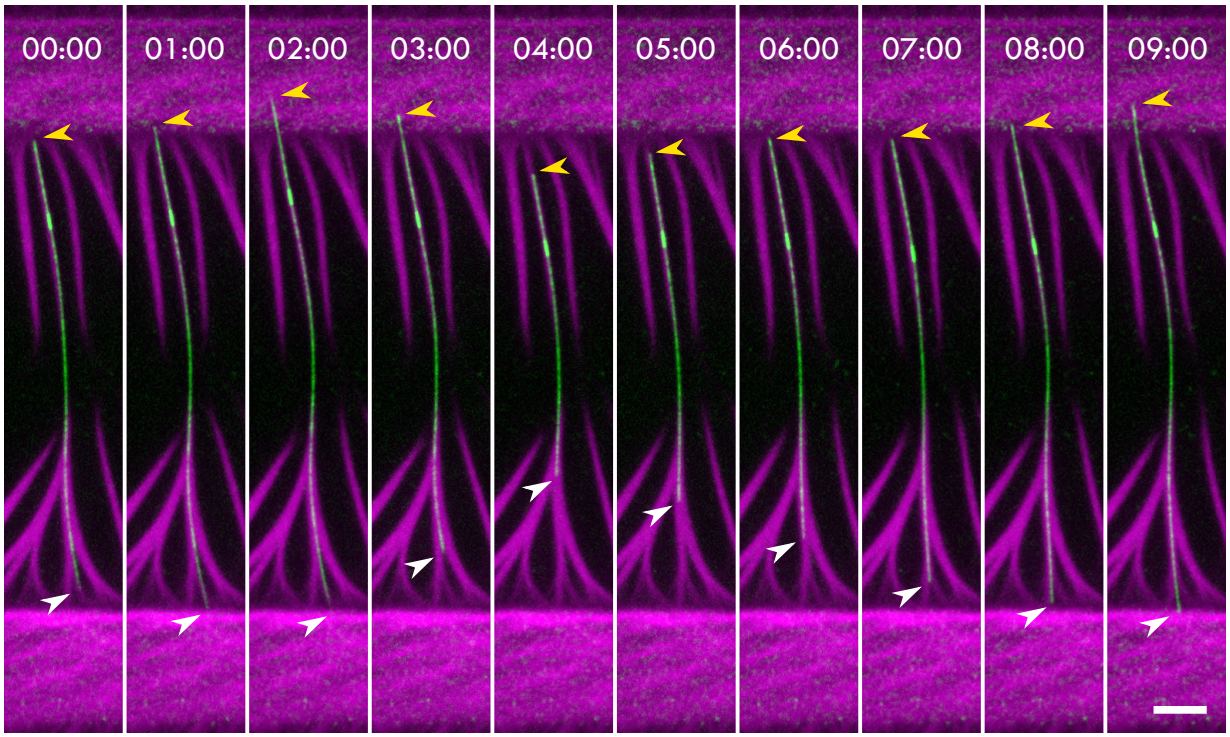

Fig. S2. Microtubule piercing from the minus end.
Time-lapse of a microtubule + tip (green, white arrow) polymerizing against a branched actin network (magenta, 10nM of Arp2/3 complex). The yellow arrow indicate the microtubule - tip. Under the pressure of polymerization the minus tip of the microtubule is able to breach inside the branched actin network. Scale bar, 5 µm.

Journal of Cell Science • Supplementary information

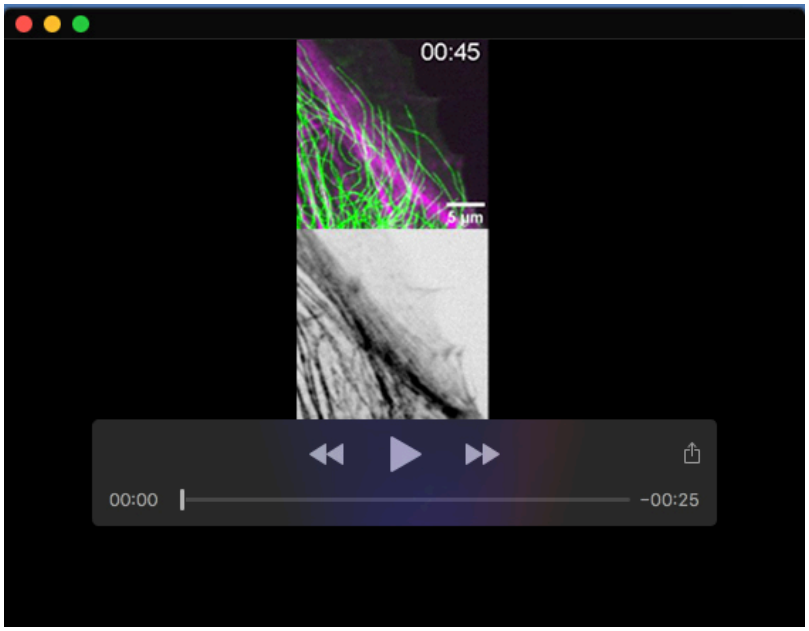

Movie 1. Example 1 of microtubules entering the lamellipodial region of cells.
Time-lapse of a PtK_2 cell tubulin-GFP (green) incubated with 200nM of SiR-actin (magenta). The movie is showing microtubules entering the lamellipodial region of the cell (Top) and the corresponding actin structure encountered along their path (bottom). Scale bar, 5 µm.

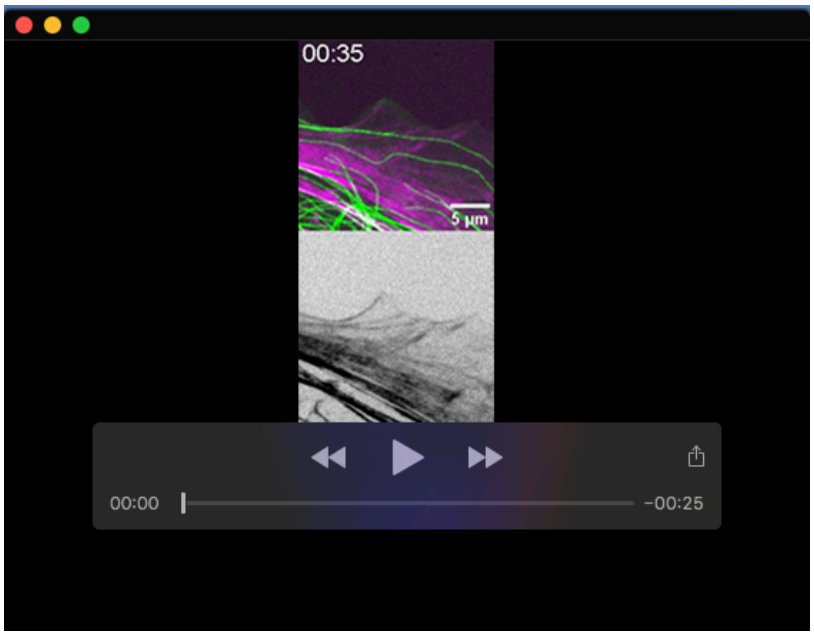

Movie 2. Example 2 of microtubules entering the lamellipodial region of cells.
Time-lapse of a PtK_2 cell tubulin-GFP (green) incubated with 200nM of SiR-actin (magenta). The movie is showing microtubules entering the lamellipodial region of the cell (Top) and the corresponding actin structure encountered along their path (bottom). Scale bar, 5 µm.

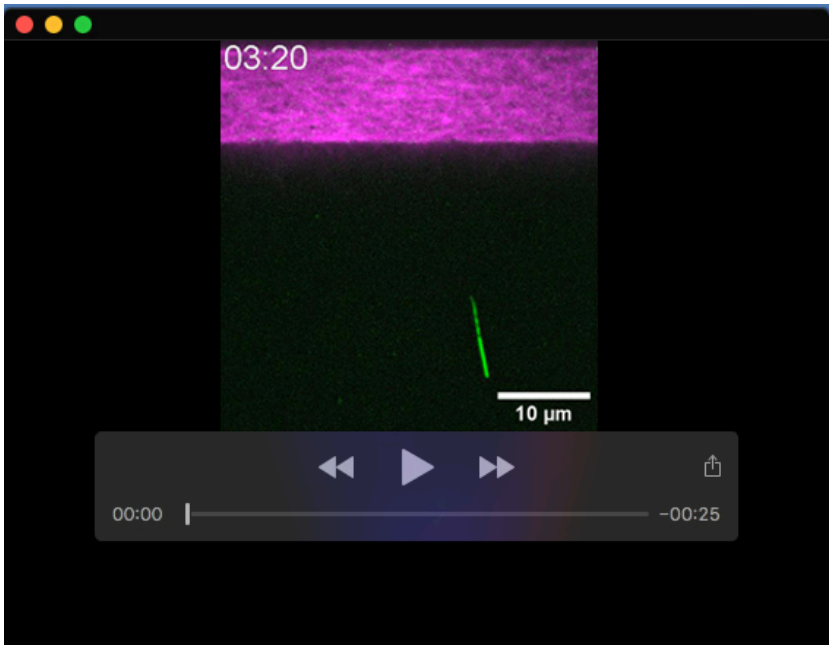

Movie 3. Dynamic microtubule polymerizing next to an actin pattern (100nM of Arp2/3 complex).
Time-lapse imaging of a dynamic microtubule (green) polymerizing next to branched actin network (magenta) in absence (100nM of Arp2/3 complex) of actin bundles. Scale bar, 10 µm.

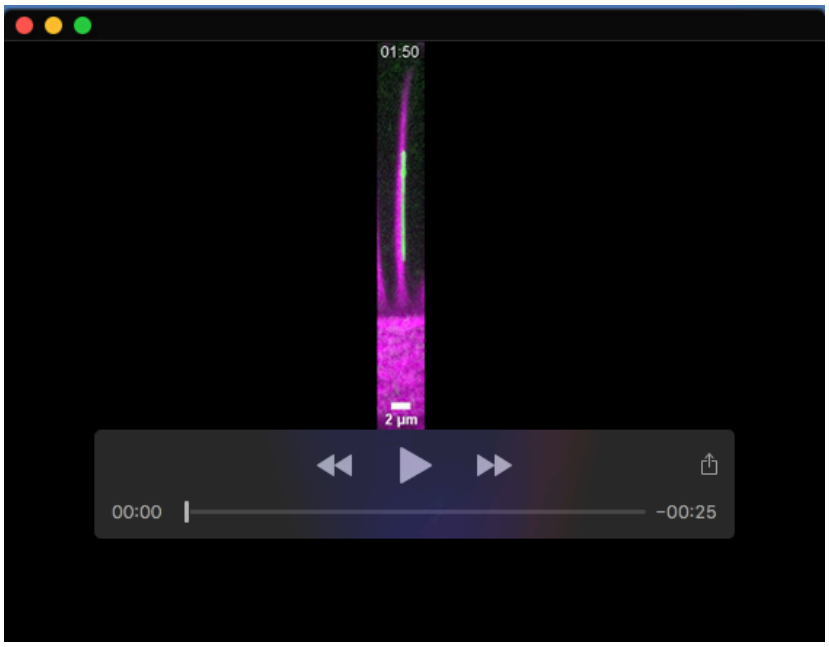

Movie 4. Dynamic microtubule polymerizing next to an actin pattern (10nM of Arp2/3 complex).
Time-lapse imaging of a dynamic microtubule (green) polymerizing next to branched actin network (magenta) in presence (10nM of Arp2/3 complex) of actin bundles. Scale bar, 10 µm.

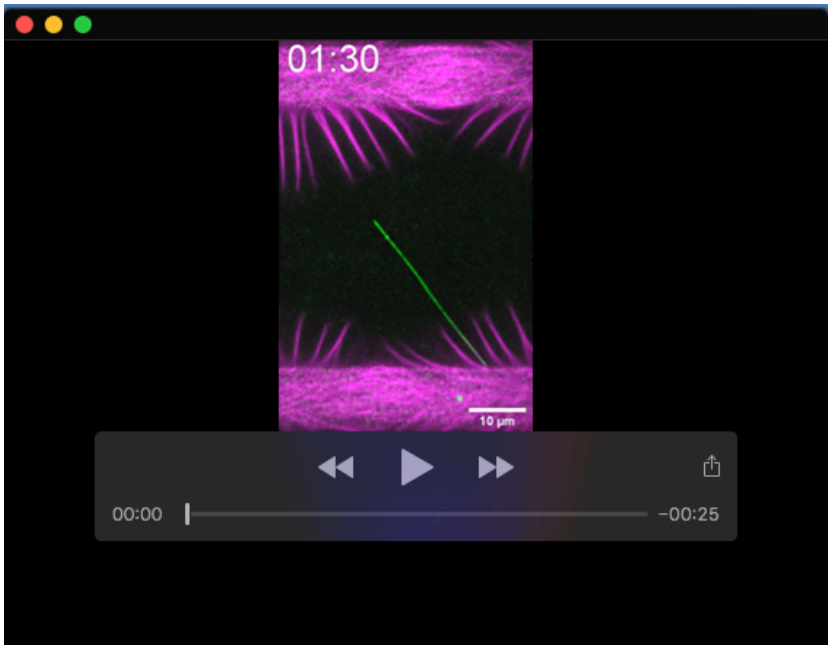

Movie 5. Dynamic microtubule breaching inside a branched actin network.
Time-lapse imaging of a dynamic microtubule (green) polymerizing in between two branched actin networks (magenta) in pres-ence of actin bundles (10nM of Arp2/3 complex). The yellow arrow shows the point of contact between the minus end of the microtubule and the branched network. The white arrow shows the plus end of the microtubule breaching inside of the branched actin network. Scale bar, 10 µm.

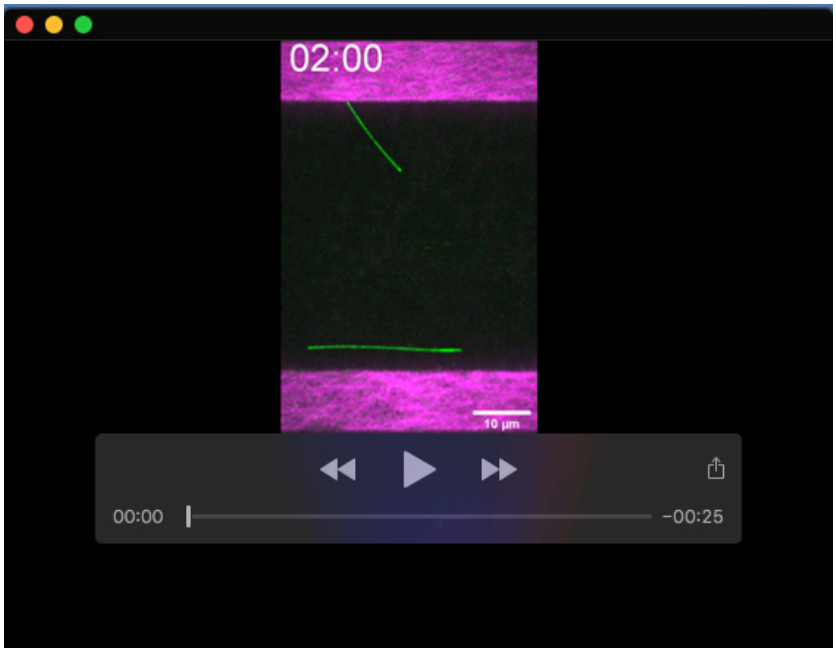

Movie 6. Dynamic microtubule not breaching inside a branched actin network.
Time-lapse imaging of dynamic microtubules (green) polymerizing in between two branched actin networks (magenta) without actin bundles (100nM of Arp2/3 complex). Scale bar, 10 µm.

Journal of Cell Science • Supplementary information

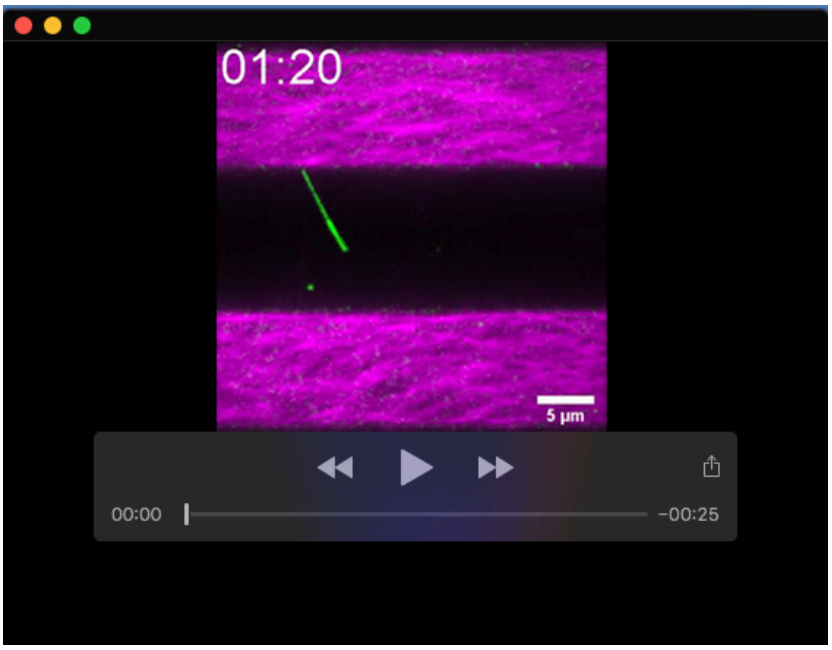

Movie 7. Dynamic microtubule polymerizing in-between close actin branched meshwork with a low angle of interaction. Time-lapse imaging of dynamic microtubules (green) polymerizing in between two branched actin networks (magenta), without actin bundles (100nM of Arp2/3 complex), at an angle lower than 60°. Scale bar, 5 µm.

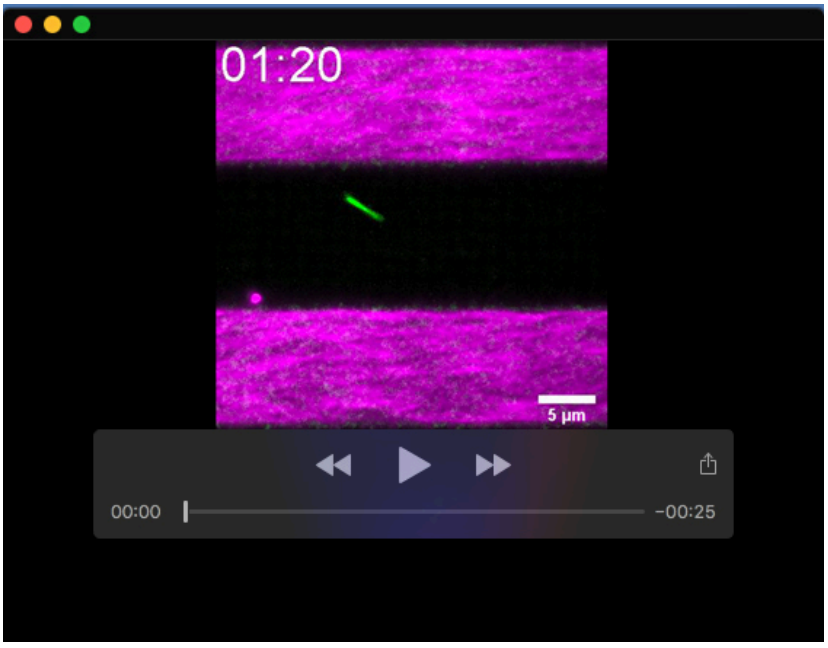

Movie 8. Dynamic microtubule polymerizing in-between close actin branched meshwork with a high angle of interaction.
Time-lapse imaging of dynamic microtubules (green) polymerizing in between two branched actin networks (magenta), without actin bundles (100nM of Arp2/3 complex), at an angle greater than 60°. Yellow arrow show the point of contact between microtubules - tip and the branched actin meshwork. White arrow show microtubule + tip piercing the branched actin meshwork. Scale bar, 10 µm.

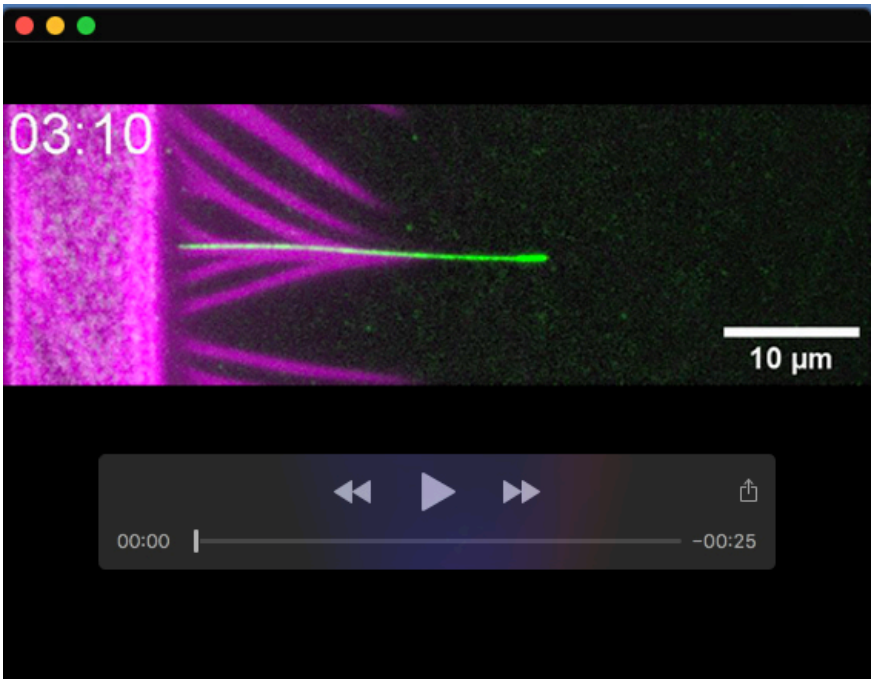

Movie 9. Dynamic microtubule polymerizing against a branched actin meshwork. Time-lapse imaging of dynamic microtubules (green) polymerizing against a branched actin network (magenta) in presence of actin bundles (10nM of Arp2/3 complex). Scale bar, 10 µm.

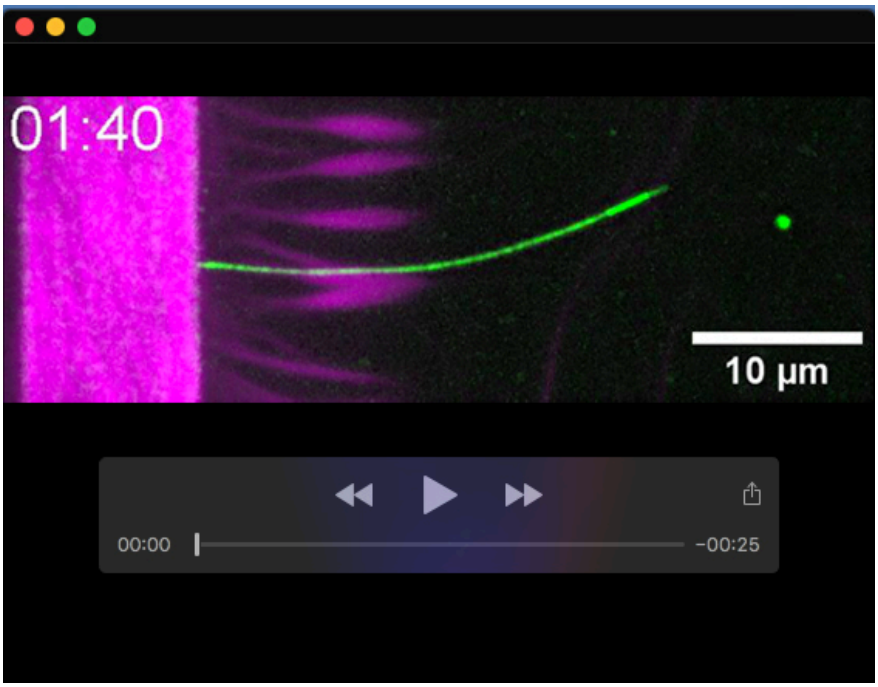

Movie 10. Dynamic microtubule polymerizing against a branched actin meshwork in presence of 100nM of Tau. Time-lapse imaging of dynamic microtubules (green) polymerizing against a branched actin network (magenta) in presence of actin bundles (10nM of Arp2/3 complex) and of an actin-microtubule crosslinker (100nM of Tau). White arrows show microtubule+ tip piercing the branched actin meshwork. Scale bar, 10 µm.

Journal of Cell Science • Supplementary information